Orbital Chern insulator at $\nu = -2$ in twisted MoTe$_2$

Feng-Ren Fan [1,2,*] Cong Xiao,[3,1,2,*] and Wang Yao[1,2,†]

[1]*Department of Physics, The University of Hong Kong, Hong Kong, China*
[2]*HKU-UCAS Joint Institute of Theoretical and Computational Physics at Hong Kong, China*
[3]*Institute of Applied Physics and Materials Engineering, University of Macau, Taipa, Macau, China*

In twisted MoTe$_2$, the latest transport measurement has reported observation of the quantum anomalous Hall effect at hole filling $\nu = -1$, which undergoes a topological phase transition to a trivial ferromagnet as layer hybridization gets suppressed by interlayer bias D. Here we show that this underlies the existence of an orbital Chern insulating state with gate (D) switchable sign in an antiferromagnetic spin background at hole filling $\nu = -2$. From momentum-space Hartree-Fock calculations, we find this state has a topological phase diagram complementary to that of the $\nu = -1$ one: by sweeping D from negative to positive, the Chern number of this $\nu = -2$ state can be switched between $+1$, 0, and -1, accompanied by a sign change of a sizable orbital magnetization. In the range of D where this antiferromagnet is the ground state, the orbital magnetization allows magnetic field initialization of the spin antiferromagnetic order and the Chern number.

Introduction. Bilayer MoTe$_2$ is a direct-gap semiconductor [1], while under twisted rhombohedral (R) stacking it hosts a honeycomb moiré superlattice with the two triangular sublattices residing on opposite layers [2,3]. From such a layer pseudospin texture, carrier motion acquires Berry phases that realize a fluxed superlattice [3,4], which underlies the Kane-Mele type topological dispersion in the lowest energy minibands [2,5]. With intrinsic ferromagnetism arising from the direct Coulomb exchange between moiré orbitals [6], such a layer-sublattice locked moiré superlattice has emerged as an exciting platform for investigating the quantum anomalous Hall (QAH) effect [7–12]. Thermodynamic evidences of both integer and fractional QAH effects were observed at hole filling of $\nu = -1$, and $\nu = -2/3, -3/5$, respectively, in twisted bilayer MoTe$_2$ (tMoTe$_2$) [7,8]. Most excitingly, with a novel contact gate design on tMoTe$_2$, direct observations of both integer and fractional QAH effects are reported in the latest transport measurements [9]. The experiments further demonstrate an electrically controlled topological phase transition at $\nu = -1$ from QAH to a trivial ferromagnet as layer hybridization gets suppressed by interlayer bias [Fig. 1(a)] [9]. These QAH transports are subsequently reproduced in an independent experiment [12].

Despite the prevailing notion that a net spin magnetization is essential for the emergence of QAH, it has been shown that the phenomenon can also be realized in collinear antiferromagnets without net spin magnetization [13–15]. In particular, a Hartree-Fock mean field calculation of the Kane-Mele Hubbard model has found a QAH phase at filling factor 2 [13] under an inversion-breaking ionic potential, which is an out-of-plane Néel antiferromagnet with zero total magnetization. This type of QAH state is reminiscent of the anomalous Hall effect in metallic antiferromagnets where the absence of combined time reversal and space inversion symmetry leads to spin splitting in Bloch bands [16–23]. The QAH effect in such phase may potentially integrate topological electronics with antiferromagnetic spintronics. However, there always exist two degenerate QAH states with opposite Néel order and Chern number, which are difficult to distinguish from the fully compensated spin magnetization, and their domain structures also hinder the observation and utilization of QAH. Alternatively, QAH can also be associated with magnetization of purely orbital nature, as indicated by the Středa formula [24] between orbital magnetization and Chern number [25]. Such orbital Chern insulator has been observed recently in magic angle twisted bilayer graphene [26–28], whereas at modest magnetic field, evidence of the fractional Chern insulator has also been reported [29].

Here we show that the experimentally observed QAH state at $\nu = -1$ filling tMoTe$_2$ underlies the existence of an orbital Chern insulator under finite interlayer bias D at $\nu = -2$, where the layer hybridization is key to the miniband topology in the layer-sublattice locked moiré. A unified momentum-space Hartree-Fock calculation reproduces the observed continuous topological phase transition of the out-of-plane ferromagnet at $\nu = -1$ (FMz) [9], and finds this $\nu = -2$ state featuring out-of-plane Néel-type spin order (AFMz) with spin-split minibands and sizable orbital magnetization. Its topological phase diagram as a function of D is essentially complementary to that of the $\nu = -1$ state [Fig. 1(b)]. At small $|D|$, either spin component occupies a layer-polarized and topologically trivial miniband, while for $|D| > D_2$, the system becomes a Chern insulator (cf. Fig. 4), as a pronounced layer hybridization is restored for one spin component due to the balance between the interlayer bias D and the Hartree

---

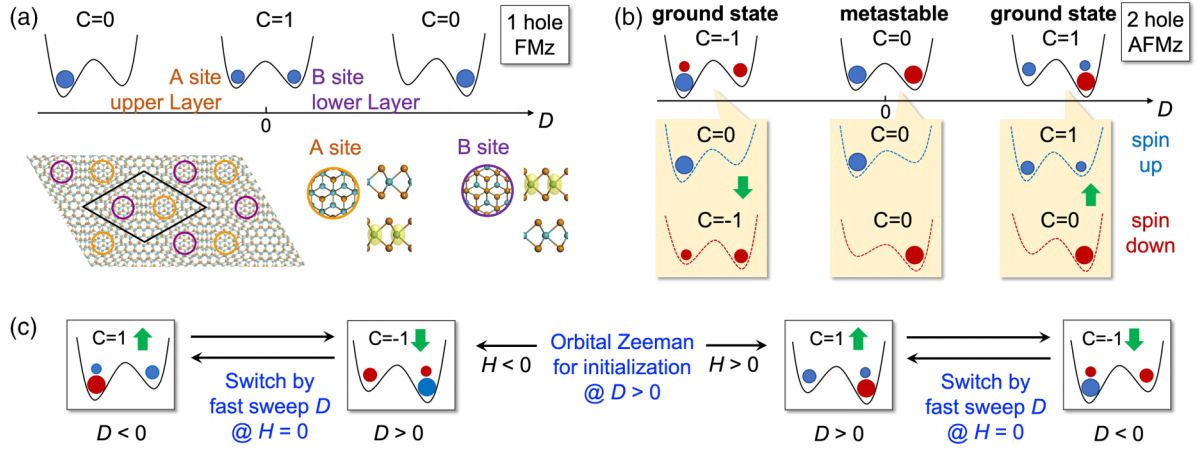*These authors contributed equally to this work.
†wangyao@hku.hk

FIG. 1. (a) Lower panel: Layer-sublattice locked honeycomb superlattice in R stacking tMoTe$_2$. The side and top views of the local stacking registries are shown for the A and B moiré sites, where holes are localized in lower and upper layer, respectively. Upper panel: Black curves illustrate the potential landscape for the two moiré sites. At filling of 1 hole per moiré cell ($\nu = -1$), the ground state is an out-of-plane ferromagnet (FMz). When the interlayer bias D is small, the FMz state is layer hybridized and exhibits the quantum anomalous Hall (QAH) effect. When $|D|$ exceeds a critical value, the FMz state becomes topologically trivial as the layer hybridization is suppressed (cf. Fig. 2). C denotes Chern number. (b) A complementary topological phase transition of an out-of-plane antiferromagnetic insulating state (AFMz) at $\nu = -2$ (cf. Figs. 3 and 4). Insets illustrate the layer wave functions, effective potentials (moiré + Hartree, dashed curves), and Chern numbers for spin up and down carriers separately. (c) In range of D where the AFMz QAH is ground state, its orbital magnetization (green arrows) allows initialization of the AFMz configurations by magnetic field H. The AFMz QAH can then be electrically switched at zero H, by sweeping D at timescale faster than spin relaxation.

potential from the other spin. By sweeping D from positive to negative, the Chern number is switched between $+1$, 0, and -1, accompanied by a sign change of orbital magnetization. In the range of D where this AFMz state is the ground state, the sizable orbital magnetization [O(0.01) μ_B/nm^2] makes possible initialization of the spin Néel order and the Chern number in applied magnetic field. And the Chern number can then be an electrically switched sign at zero magnetic field, by sweeping D at a timescale faster than magnetic relaxation [Fig. 1(c)]. These findings imply new possibilities for antiferromagnetic spintronics and topological electronics based on layer-sublattice locked moiré in twisted transition metal dichalcogenides (TMDs).

Method. To describe the spontaneous time-reversal-symmetry breaking from electron-electron interactions, we employ self-consistent momentum (k)-space Hartree-Fock calculations based on the continuum model for twisted R stacking homobilayer TMDs. The Hartree-Fock mean-field Hamiltonian reads

$$H_{\mathrm{HF}} = H_0 + H_{\mathrm{int}}, \tag{1}$$

where H_0 is the single-particle continuum Hamiltonian [2]

$$H_0 = \begin{pmatrix} h_k^t - \frac{E_D}{2} & w \\ w^\dagger & h_k^b + \frac{E_D}{2} \end{pmatrix}, \tag{2}$$

where $h_k^\alpha = -\frac{(k - K^\alpha)^2}{2m_\alpha} + V_k^\alpha$ is the single-layer Hamiltonian near valley K^α in layer α, $E_D = Dd_0/\epsilon$ is the energy difference caused by the interlayer bias D, with d_0 and ϵ being respectively the interlayer distance and relative dielectric constant, V_k^α the Fourier transformation of the intralayer moiré potential $V^\alpha(\mathbf{r}) = -2V_0 \sum_{i=1,3,5} \cos(\mathbf{g}_i \cdot \mathbf{r} + \phi_\alpha)$, and $w(\mathbf{r}) = w_0(1 + e^{i\mathbf{g}_2 \cdot \mathbf{r}} + e^{i\mathbf{g}_3 \cdot \mathbf{r}})$ their interlayer tunneling. $\mathbf{g}_i$ is the first-shell moiré reciprocal vectors. The model parameters for tMoTe$_2$

are $m_t = m_b = -0.62m_e$ [2], $V_0 = 20.82$ meV, $\phi_t = -\phi_b = -107.7°$, and $w = -23.8$ meV [30]. H_{int} in Eq. (1) is the interaction term which, based on the plane-wave basis expanded by the moiré reciprocal lattice vectors, reads

$$H_{\mathrm{int}} = \frac{1}{2\Omega} \sum_{k,k',q,\alpha\beta,\tau\tau'} V_{\alpha\beta}(q) c_{k+q,\alpha\tau}^\dagger c_{k'-q,\beta\tau'}^\dagger c_{k',\beta\tau'} c_{k,\alpha\tau}. \tag{3}$$

Here τ is the valley index, and $V_{\alpha\beta}$ is the Coulomb interaction taking the form $V_{\alpha\beta}(q) = \frac{2\pi e^2}{\epsilon q} e^{-qd_0(1-\delta_{\alpha\beta})}$, with $\delta_{\alpha\beta}$ being the Kronecker delta.

H_0 features the Kane-Mele type topological dispersion in its lowest two minibands [2], which are predominantly accounted for by two moiré orbitals residing on opposite layers [cf. Fig. 1(a)], forming a honeycomb superlattice where the Berry phase from the layer texture realizes the flux needed in the Kane-Mele model [3]. Earlier work based on the two-orbital Kane-Mele Hubbard model found that the ground state at filling 2 is an AFMz QAH at a range of finite ionic potential Δ_{AB} that lifts the A-B sublattice [Fig. 1(a)] degeneracy, which undergoes a magnetic phase transition with the decrease of Δ_{AB} [13], becoming a trivial in-plane antiferromagnet (AFMxy) in the neighbourhood of $\Delta_{AB} = 0$ [31,32]. Hartree-Fock calculations from Eq. (1) can produce these spin magnetic orders with qualitatively the same dependence on interlayer bias D [33].

On the other hand, the moiré orbitals here are rather extended in the shallow confinement which also varies significantly with D, and their direct Coulomb exchange, absent in the Kane-Mele Hubbard model [13], is responsible for the observed FMz QAH at $\nu = -1$ [6]. A k-space Hartree-Fock treatment keeping a large number of minibands is necessitated to properly account for the subtle D dependence of the spatial and layer wave function, as well as the orbital magnetization.
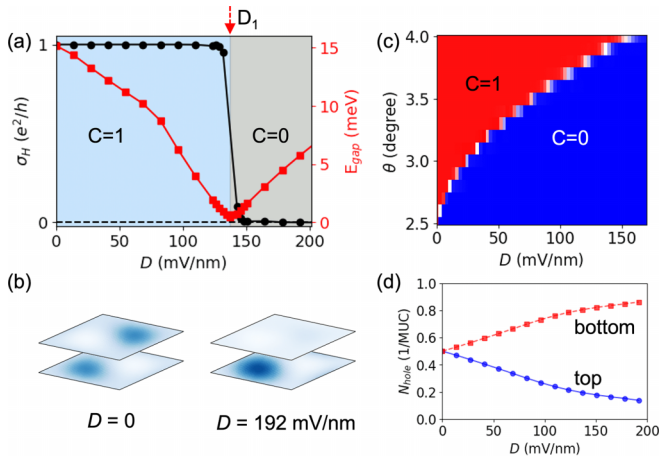
FIG. 2. (a) The variation of anomalous Hall conductivity and band gap as functions of interlayer bias D, with twist angle $\theta = 3.9°$. The black-circle line represents the Hall conductivity, while the red-square line the band gap. The background colors denote the Chern number. $D_1 = 137$ mV/nm is the topological transition point. (b) The layer distribution of the doped hole under interlayer bias $D = 0$, and $D = 192$ mV/nm. (c) Phase diagram of 1-hole doped tMoTe$_2$, as a function of twist angle and interlayer bias. (d) Number of holes per moiré unit cell (MUC) on each layer under different interlayer bias. The blue-circle line denotes the top layer, whereas the red-square line the bottom layer.
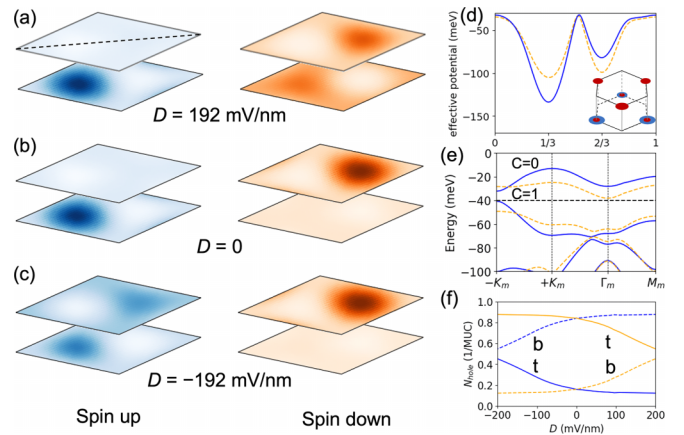

FIG. 3. (a)–(c) Layer distribution of wave functions for the $\nu = -2$ AFMz states under interlayer bias $D = 192$ mV/nm, 0, and -192 mV/nm, respectively. (d) Effective potentials (moiré + Hartree) along the long diagonal of the moiré cell [cf. panel (a)] for spin-up and spin-down holes, respectively, at $D = 192$ mV/nm. Inset is a schematic of magnetic configuration. Spin-up and spin-down holes are denoted by blue and red circles, respectively, with the size representing the population. In (d)–(f), blue (orange) color denotes spin up (down). (e) Quasiparticle band dispersion of the $\nu = -2$ AFMz state under interlayer bias $D = 192$ mV/nm. (f) Dashed (solid) curves denote number of holes per MUC in top (bottom) layer.

The calculations presented below have considered 148 minibands for each spin component. The orbital magnetization is calculated following Ref. [34].

QAH state at filling $\nu = -1$. We first show the calculation results at hole filling $\nu = -1$, of which the magnetic and topological properties have recently been studied in experiment [6,9]. Figure 2(a) depicts the variation of anomalous Hall conductivity of 3.9° tMoTe$_2$ as a function of interlayer bias. The Hall conductivity exhibits a jump from e^2/h to 0 at the critical interlayer bias $D_1 \sim 140$ mV/nm, indicating a topological phase transition. The band gap, denoted by red squares, varies continuously and closes at the transition point. In addition, there is an inflection point of the band gap near $D \sim 75$ mV/nm, which is a result of the band gap transition from a direct type to an indirect type. All these features are consistent with the observation of bias-driven topological transition in a recent experiment [9].

Such a bias-driven topological transition is correlated with the change of layer wave function of the doped hole. Figure 2(b) demonstrates the layer distribution of the probability density of the doped hole in the topologically nontrivial state at $D = 0$ and the topologically trivial state at $D = 192$ mV/nm. At $D = 0$, the distribution of doped holes is hybridized between the two layers. Because of the layer-sublattice locking, the doped hole is also equally distributed on sublattices A and B [Fig. 1(a)]. In contrast, at $D = 192$ mV/nm, the doped hole is mainly distributed on the bottom layer, being a topologically trivial system with vanishing Chern number. Figure 2(d) shows the variation of the number of holes on each layer as a function of interlayer bias. As the bias increases, the system transforms from a fully layer-hybridized state to a strongly layer-polarized state.

We also explore the twist-angle dependence of the critical bias for the topological transition by showing the phase diagram in Fig. 2(c). One finds that the critical bias increases with the twist angle. This is anticipated as the low-energy bandwidth increases with the twist angle, diminishing the effect of bias tuning.

Bias-tunable orbital Chern insulator at $\nu = -2$. The above understanding of the filling $\nu = -1$ state enables exploring the bias-controlled topological properties of the $\nu = -2$ AFMz state in tMoTe$_2$, as indicated in Fig. 1. At $D = 0$, each sublattice hosts a hole with opposite spin, as depicted in Fig. 3(b). Each spin species is essentially the same as the topologically trivial $\nu = -1$ state with strong layer polarization [right panel of Fig. 2(b)]. When an interlayer bias is applied, one of the spin species starts to be driven to the other layer, becoming more layer-hybridized, while the other spin species remains layer-polarized, as shown in Figs. 3(a) and 3(c). The effective potentials (moiré + Hartree) for the two spin species at $D = 192$ mV/nm are displayed in Fig. 3(d), where the potential well for the spin-down hole is balanced by the applied bias and Hartree potential. Figure 3(f) illustrates the number of holes on each layer varying with the bias. When D increases on the positive axis, the layer distribution of the spin-up hole (blue lines) changes little, while the spin-down hole (orange lines) becomes layer hybridized. Conversely, when $D < 0$, the spin-up hole becomes layer hybridized. In line with the case of the $\nu = -1$ state, such layer-hybridized insulating states are expected to be topologically nontrivial, which is indeed confirmed by our calculations. As shown in Fig. 4(a), when $|D|$ increases, the Chern number jumps from 0 to 1 or -1, depending on the sign of the bias. Such jumps signal bias-driven topological phase transitions [Fig. 4(b)]. Figure 4(d) shows the topological phase diagram of the AFMz
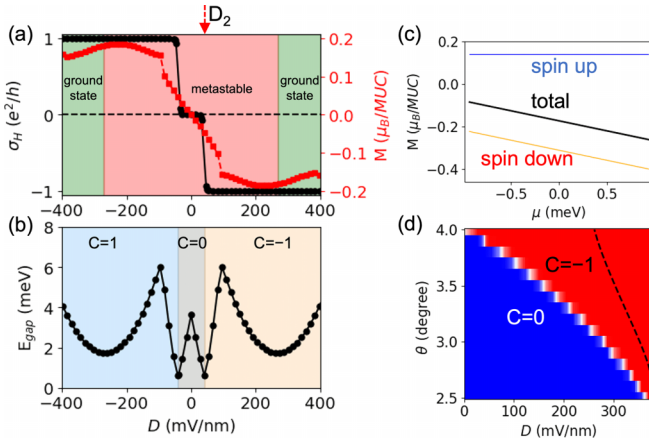
FIG. 4. (a) The anomalous Hall conductivity (black circles) and orbital magnetization (red squares) as functions of interlayer bias in the $\nu = -2$ AFMz state with twist angle $\theta = 3.9°$. The background color denotes region where AFMz is the ground state (green) or metastable (red). (b) The band gap of AFMz state as a function of interlayer bias. Gap closing occurs at the transition points. (c) Orbital magnetization of the $\nu = -2$ AFMz state, under interlayer bias $D = 300$ mV/nm, as a function of chemical potential μ that varies inside the gap. The blue and orange lines are the orbital magnetization contributed by spin-up and spin-down holes, respectively, and the black line is their sum. (d) Topological phase diagram of the $\nu = -2$ AFMz state, as a function of twist angle and interlayer bias. The AFMz state is the ground state to the right side of black dashed curve, and is metastable to the left.

state as a function of twist angle and interlayer bias. As the twist angle decreases, the critical bias for the topological phase transition increases. This behavior is opposite to that of the $\nu = -1$ case as the transition here is reversed, i.e., from layer-polarized (topologically trivial) to layer-hybridized (topologically nontrivial) states.

Next, we reveal the magnetic properties of this bias-driven Chern insulator. The nonvanishing Hall conductivity implies that the symmetry of the system supports time-reversal odd pseudovectors in the out-of-plane direction, thus a nonzero net magnetization. However, the insulating gap protects the fully compensated spin magnetic order [13] even when the bias is applied, as is verified by Fig. 3(d) as well. As such, the net magnetization can only be of orbital origin. This scenario is corroborated by the calculation results shown in Fig. 4(a). The induced orbital magnetization depends linearly on the bias when the latter is small, and reaches the order of $0.01 \ \mu_B/\text{nm}^2$ in the topologically nontrivial phase. Such a sizable value is well within the capacity of magneto-optical experiment and is comparable to that observed in twisted bilayer graphene [35]. Moreover, in the topologically nontrivial phase the orbital magnetization changes linearly with respect to the chemical potential within the gap [Fig. 4(c)], and the slope is quantified by the Chern number in accordance with the

Středa formula [24], i.e., $dM/d\mu = Ce/2\pi\hbar$, where M is orbital magnetization and C is the Chern number. This character offers a feasible approach to experimental identification of the Chern insulator without the need of applying magnetic field. In Fig. 4(a), the values of M are taken at the middle of band gap at each D, and the non-differentiable points at finite D are due to the change from direct to indirect band gap [cf. the sharp turning in Fig. 4(b)].

Discussion and outlook. In MoTe$_2$, the spin direction from each valley is out of plane. For tMoTe$_2$ at filling factor $\nu = -2$, at $D = 0$, the intravalley Fock exchange induces valley coherence [36], resulting in an in-plane spin magnetic configuration (AFMxy) as the ground state [13,32,33]. The interlayer bias lifts the spin degeneracy and weakens the valley coherence, stabilizing the AFMz state which becomes the ground state at a range of finite D [13,33]. Starting from this AFMz phase at a finite bias (e.g., $D > 0$), and upon fast-switching the bias direction, the system will go through the neighborhood of $D = 0$ where AFMxy is the ground state and the AFMz state is metastable [cf. Figs. 4(a) and 4(d)]. Nevertheless, as the magnetic relaxation could be slow as compared to the electrical sweep, the system can remain in the AFMz configuration and undergo the continuous topological transition, ending at the AFMz ground state of opposite Chern number at $D < 0$, thus allowing an electrically controlled sign switch of the Chern number.

The magnetic state studied here has some interesting connections to the concept of altermagnetism [16–23]. For this concept, three main features have been noted in the literature: (1) compensated collinear spin order, (2) spin-splitting band structure or alternating spin polarization in k space, and (3) a certain rotation symmetry connecting sublattices with opposite spin. The first two features underly the novel response properties of altermagnets, such as the spin-splitting torque [37,38], while (3) serves as a symmetry constraint guaranteeing (1) [18–20]. The topological magnetic state discovered at $\nu = -2$ tMoTe$_2$ here has the first two features, but the spin-up and spin-down channels are not related by rotation symmetry. Therefore, the $\nu = -2$ tMoTe$_2$ here has some similarities to but is different from the altermagnetic system. The sizable orbital magnetization here allows for efficient magnetic-field control and switch of the two time-reversed degenerate topological states, e.g., for initialization of a designated magnetic state with definite Chern number. With such controllability through bias and magnetic field, the twisted TMD bilayers provide a promising platform for manipulations of topological magnetism.

[1] I. G. Lezama, A. Arora, A. Ubaldini, C. Barreteau, E. Giannini, M. Potemski, and A. F. Morpurgo, Nano Lett. **15**, 2336 (2015).

[2] F. Wu, T. Lovorn, E. Tutuc, I, Martin, and A. H. MacDonald, Phys. Rev. Lett. **122**, 086402 (2019).

[3] H. Yu, M. Chen, and W. Yao, Natl. Sci. Rev. **7**, 12 (2020).

[4] D. Zhai and W. Yao, Phys. Rev. Mater. **4**, 094002 (2020).

[5] T. Devakul, V. Crépel, Y. Zhang, and L. Fu, Nat. Commun. **12**, 6730 (2021).

[6] E. Anderson, F.-R. Fan, J. Cai, W. Holtzmann, T. Taniguchi, K. Watanabe, D. Xiao, W. Yao, and X. Xu, Science **381**, 325 (2023).

[7] J. Cai, E. Anderson, C. Wang, X. Zhang, X. Liu, W. Holtzmann, Y. Zhang, F.-R. Fan, T. Taniguchi, K. Watanabe, Y. Ran, T. Cao, L. Fu, D. Xiao, W. Yao, and X. Xu, Nature (London) **622**, 63 (2023).

[8] Y. Zeng, Z. Xia, K. Kang, J. Zhu, P. Knüppel, C. Vaswani, K. Watanabe, T. Taniguchi, K. F. Mak, and J. Shan, Nature (London) **622**, 69 (2023).

[9] H. Park, J. Cai, E. Anderson, Y. Zhang, J. Zhu, X. Liu, C. Wang, W. Holtzmann, C. Hu, Z. Liu, T. Taniguchi, K. Watanabe, J.-h. Chu, T. Cao, L. Fu, W. Yao, C.-Z. Chang, D. Cobden, D. Xiao, and X. Xu, Nature (London) **622**, 74 (2023).

[10] B. A. Foutty, C. R. Kometter, T. Devakul, A. P. Reddy, K. Watanabe, T. Taniguchi, L. Fu, and B. E. Feldman, arXiv:2304.09808.

[11] H. Li, U. Kumar, K. Sun, and S.-Z. Lin, Phys. Rev. Res. **3**, L032070 (2021).

[12] F. Xu, Z. Sun, T. Jia, C. Liu, C. Xu, C. Li, Y. Gu, K. Watanabe, T. Taniguchi, B. Tong, J. Jia, Z. Shi, S. Jiang, Y. Zhang, X. Liu, and T. Li, Phys. Rev. X **13**, 031037 (2023).

[13] K. Jiang, S. Zhou, X. Dai, and Z. Wang, Phys. Rev. Lett. **120**, 157205 (2018).

[14] W.-B. Dai, H. Li, D.-H. Xu, C.-Z. Chen, and X. C. Xie, Phys. Rev. B **106**, 245425 (2022).

[15] P.-J. Guo, Z.-X. Liu, and Z.-Y. Lu, npj Comput. Mater. **9**, 70 (2023).

[16] S. Hayami, Y. Yanagi, and H. Kusunose, J. Phys. Soc. Jpn. **88**, 123702 (2019).

[17] D.-F. Shao, S.-H. Zhang, M. Li, C.-B. Eom, and E. Y. Tsymbal, Nat. Commun. **12**, 7061 (2021).

[18] L. Šmejkal, J. Sinova, and T. Jungwirth, Phys. Rev. X **12**, 031042 (2022).

[19] L. Šmejkal, J. Sinova, and T. Jungwirth, Phys. Rev. X **12**, 040501 (2022).

[20] I. Mazin, Phys. Rev. X **12**, 040002 (2022).

[21] L. Šmejkal, A. H. MacDonald, J. Sinova, S. Nakatsuji, and T. Jungwirth, Nat. Rev. Mater. **7**, 482 (2022).

[22] Z. Feng, X. Zhou, L. Šmejkal, L. Wu, Z. Zhu, H. Guo, R. González-Hernández, X. Wang, H. Yan, P. Qin, X. Zhang, H. Wu, H. Chen, Z. Meng, L. Liu, Z. Xia, J. Sinova, T. Jungwirth, and Z. Liu, Nat. Electron. **5**, 735 (2022).

[23] R. D. Gonzalez Betancourt, J. Zubac, R. Gonzalez-Hernandez, K. Geishendorf, Z. Soban, G. Springholz, K. Olejnik, L. Smejkal, J. Sinova, T. Jungwirth, S. T. B. Goennenwein, A. Thomas, H. Reichlova, J. Zelezny, and D. Kriegner, Phys. Rev. Lett. **130**, 036702 (2023).

[24] P. Streda, J. Phys. C: Solid State Phys. **15**, L717 (1982).

[25] J. Zhu, J.-J. Su, and A. H. MacDonald, Phys. Rev. Lett. **125**, 227702 (2020).

[26] A. L. Sharpe, E. J. Fox, A. W. Barnard, J. Finney, K. Watanabe, T. Taniguchi, M. A. Kastner, and D. Goldhaber-Gordon, Science **365**, 605 (2019).

[27] M. Serlin, C. L. Tschirhart, H. Polshyn, Y. Zhang, J. Zhu, K. Watanabe, T. Taniguchi, L. Balents, and A. F. Young, Science **367**, 900 (2020).

[28] H. Polshyn, J. Zhu, M. A. Kumar, Y. Zhang, F. Yang, C. L. Tschirhart, M. Serlin, K. Watanabe, T. Taniguchi, A. H. MacDonald, and A. F. Young, Nature (London) **588**, 66 (2020).

[29] Y. Xie, A. T. Pierce, J. M. Park, D. E. Parker, E. Khalaf, P. Ledwith, Y. Cao, S. H. Lee, S. Chen, P. R. Forrester, K. Watanabe, T. Taniguchi, A. Vishwanath, P. Jarillo-Herrero, and A. Yacoby, Nature (London) **600**, 439 (2021).

[30] C. Wang, X.-W. Zhang, X. Liu, Y. He, X. Xu, Y. Ran, T. Cao, and D. Xiao, arXiv:2304.11864.

[31] M. Hohenadler, Z. Y. Meng, T. C. Lang, S. Wessel, A. Muramatsu, and F. F. Assaad, Phys. Rev. B **85**, 115132 (2012).

[32] W.-X. Qiu, B. Li, X.-J. Luo, and F. Wu, Phys. Rev. X **13**, 041026 (2023).

[33] X. Liu, C. Wang, X.-W. Zhang, T. Cao, and D. Xiao, arXiv:2308.07488.

[34] D. Xiao, M.-C. Chang, and Q. Niu, Rev. Mod. Phys. **82**, 1959 (2010).

[35] C. L. Tschirhart, M. Serlin, H. Polshyn, A. Shragai, Z. Xia, J. Zhu, Y. Zhang, K. Watanabe, T. Taniguchi, M. E. Huber, and A. F. Young, Science **372**, 1323 (2021).

[36] J. Liu and X. Dai, Phys. Rev. B **103**, 035427 (2021).

[37] H. Bai, L. Han, X. Y. Feng, Y. J. Zhou, R. X. Su, Q. Wang, L. Y. Liao, W. X. Zhu, X. Z. Chen, F. Pan, X. L. Fan, and C. Song, Phys. Rev. Lett. **128**, 197202 (2022).

[38] A. Bose, N. J. Schreiber, R. Jain, D.-F. Shao, H. P. Nair, J. Sun, X. S. Zhang, D. A. Muller, E. Y. Tsymbal, D. G. Schlom, and D. C. Ralph, Nat. Electron. **5**, 267 (2022).